In situ genesis of selective adsorption sites by complex catalytic redox dynamics

Luis Sandoval-Diaz
Fritz Haber Institute of the Max Planck Society
Daniel Cruz
Fritz Haber Institute of the Max Planck Society
Thomas Götsch
Fritz Haber Institute of the Max Planck Society
Milivoj Plodinec
Fritz Haber Institute of the Max Planck Society
Adnan Hammud
Fritz Haber Institute of the Max Planck Society
Danail Ivanov
Fritz Haber Institute of the Max Planck Society
Michael Hävecker
Fritz Haber Institute of the Max Planck Society
Robert Schlögl
Fritz Haber Institute of the Max Planck Society
Axel Knop-Gericke
Fritz-Haber-Institut der Max-Planck-Gesellschaft
Thomas Lunkenbein (✉ lunkenbein@fhi-berlin.mpg.de)
Fritz Haber Institute of the Max Planck Society https://orcid.org/0000-0002-8957-4216

Article

Keywords:

Posted Date: November 29th, 2022

DOI: https://doi.org/10.21203/rs.3.rs-2259845/v1

Abstract

Several *in situ* studies have revealed spatiotemporal dynamics on heterogeneous catalysts surfaces under chemical stimuli[1-4], which presumably control the activity, selectivity, and productivity[5-11]. However, *operando* validations of sufficient spacetime resolution[12] are often missing, and hence, the effect of these dynamics on catalytic performance may not be entirely clear. Here, using dry reforming of methane over Ni as an example, we demonstrate the relevance of catalytic redox dynamics for reaction performance and determine their genesis from adaptive chemistry and continual catalytic cycling. By combining *operando* scanning electron microscopy and near-ambient-pressure X-ray photoelectron spectroscopy, we found that activation sites for methane and carbon dioxide differed but continually transformed into each other during the reaction. This behavior enabled a self-sustained oscillating regime evincing the sequential formation of active sites. We also found that not all spatiotemporal dynamics accounted for the catalytic function. We highlight the importance of oscillating reactions for mechanistic studies and propose that the generation of mechanical strain at the catalyst during redox cycling acted as a feedback element for the oscillations. These observations lead to deeper understanding of fundamental catalysis and open new opportunities for tuning catalytic performances.

1. Main

Heterogeneous catalysts dynamics under reaction conditions include overlayer formation/depletion on nanoparticles[3], reshapings[4,5], sintering[6], spatiotemporal patterns (oscillations, chemical wave fronts),[7–9] and phase transitions[10–12]. In this context, modern electron microscopes are key for in situ assessments of these dynamics thanks to their powerful space resolution. However, fundamental understanding about the role of such dynamics on reaction performance may still be lacking. One reason is that most of the studies in this field have focused on the dynamics, but in situ information about reaction observables has been relegated to a secondary level[4,13,14]. Consequently, only few operando studies have been accomplished in electron microscopy and have restrained their application to simple reactions of the automotive catalytic converter, such as H_2 or CO oxidation[11,14,15]. Here, we explore the intricate relationship between various catalytic dynamics and the catalytic functioning of a metallic Ni catalyst in the complex chemical network (Extended Data Table 1) of dry reforming of methane (DRM) by correlative operando analysis.

We initially investigated the impact of different gas environments on the catalyst surface at temperatures relevant for DRM. For this, we treated the catalyst in our operando scanning electron microscopy (OSEM) setup using a H_2:Ar feed. The reduced surface appeared flat and smooth without reconstructions (Fig. 1a, 1b top, 1c top). Near-ambient-pressure X-ray photoelectron spectroscopy (NAP-XPS) characterizations corroborate the Ni reduced state during this treatment at varying depth sensitivities (Extended Data Fig. 1a). Both techniques point to the presence of SiO_x particles decorating the reduced Ni surface (see arrows in Fig. 1).

Bright nanometric features (Fig. 1b) were formed on the surface after replacing H_2 in the feed with CO_2. Correlatively, increasing O1s signals and a transition from Ni^0 (BE = 852.4 eV) into Ni^{2+} (856.2 eV) were detected by NAP-XPS measurements (Extended Data Fig. 1b). C-containing species were absent. In contrast, no changes were observed neither in OSEM images (Fig. 1c) nor in NAP-XP spectra (Extended Data Fig. 1c) when the feed was switched from H_2 into CH_4, implying a clean metallic state with coking preclusion. In brief, the catalyst oxidized in CO_2 feed, but remained in the reduced state without coking in CH_4 atmosphere. Deconvolution of O1s XPS lines in the CO_2:Ar atmosphere (Extended Data Fig. 2a) unravels at least two contributions of nickel oxides, which we interpret as NiO (binding energy, BE = 529.4 eV), and poorly characterized defective phases of NiO_d (BE = 531.3 eV) including non-stoichiometric, ill-defined or layered phases such as $Ni_{2-x}O_{3-y}$ or NiOOH[16]. We will refer to all NiO_x phases as *oxides*.

We investigated then the catalyst states under a fixed composition of DRM feed (CO_2:CH_4:Ar) at temperatures between 700°C and 900°C. The reaction mixture oxidized the surface below 808°C (bright features in Figs. 2a and 2b). Between 808°C and 825°C, the previously formed oxides were consumed (compare Figs. 2b and 2c). The redox transition corresponding to surface reduction was apparently completed at 825°C. The catalyst remained seemingly metallic at temperatures between 825°C and 900°C (Fig. 2d). These observations were validated with simultaneous information about catalytic performance. While increasing OSEM image intensities indicating surface oxidation were detected below 808°C (Fig. 2e), conversions to H_2, CO and H_2O were small with H_2/CO ratios below 1.0. During surface reduction, OSEM image intensities decreased abruptly. Simultaneously, water and syngas (H_2 + CO) productions ignited (Fig. 2e, gray area), with H_2/CO ratios above 1.0 and pronounced H_2O production. These trends continued above 825°C, until H_2O formation decreased and H_2/CO ratios slowly approached 1.0 after 1000 minutes of treatment at 900°C[17]. Surface reduction and absence of C-containing species during catalytic activation were determined by NAP-XPS measurements (Figs. 2f, Extended Data Figs. 2b and 3) at conditions similar to those of OSEM.

In brief, surface oxidation and little activity dominated below 808°C, while the active surface was mostly reduced above 825°C. Note that the influence of the redox transition on the reaction mechanism remains puzzling with only these observations. To understand its role, reaction rates and redox dynamics need to be adjusted for suitable inspection. In the following, we explore the system behavior during the phase transition, in which surface redox changes may reach spatiotemporal magnitudes sufficient for evaluation with detectable activity (gray area, Fig. 2e).

After 1000 minutes at 900°C in the DRM feed, the catalyst temperature was decreased to 817°C. Differently shaped oxides reappeared on the surface, indicating the reversibility of the redox transition and the irreversibility of local morphologies over the long term (Fig. 3). Remarkably, oscillatory dynamics corresponding to periodic cycles of oxide growth and shrinkage initiated spontaneously after 10 minutes (Extended Data Video 1) although heating power and gas feeds were kept constant.

We followed the oscillations for 15 hours. Figures 3a to 3f exemplify the gradual depletion and subsequent growth of oxides on determined surface locations. Reactants, products, H_2/CO ratios, and oxide contents represented by OSEM image intensities, oscillated in phase, with a 93 minutes period (Figs. 3g and 3h). Oxides fluctuated on discrete locations, which could be attributed to a pinning influence of nanometric silica (Fig. 1, Extended Data Fig. 1, 2). Minima in production rates occurred simultaneously to maxima in OSEM image intensities, i.e., at the largest oxide coverages.

We define 3 instants in the oscillating traces (Fig. 3h): Instant 1, corresponding to the beginning of oxide growth. Decreasing catalytic rates and H_2/CO ratios were characteristic at this instant. Image intensities peaked in a maximum at instant 2, with a minimum of catalytic activities and H_2/CO ratios. Afterwards, image intensities rapidly decreased accompanied by fast catalytic reactivation and increasing H_2/CO ratios. Production rates reached a maximum at instant 3. Subsequently, the reaction slowly deactivated (H_2/CO = 1.0) until the system reached instant 1 of the next cycle.

Self-sustained oscillations are not an exception in a variety of static catalyst operations. Rather, they represent the rarely synchronized manifestation of regular dynamic operation achieved by fine coupling of reaction rates. They also give access to detailed mechanistic information as the spacetime amplitude of the dynamics reaches magnitudes suitable for the observer resolution. Periodic autocorrelation functions of the oscillations (Fig. 4a) reveal an intermediate signal in the trace of image intensities, which was neither related to oxide contents nor to activity. Extended Data Fig. 4 and Video 2 show that the metallic surface which remained free of oxides underwent periodic reconstruction, “smoothening”, and “roughening” cycles between the main oscillations. Before reaching instant 1, the smooth metallic surface reconstructed and “roughened”. At instant 1, the reconstructed catalyst underwent oxide formation. Instant 2 exhibited the highest oxide contents and “roughening” of the metallic part. A few minutes after the shrinkage of the oxides at instant 3, the metallic surface “smoothened” again. These results suggest that the intermediate signal of Fig. 1a related to localized surface reconstructions inducing slight variations in OSEM image intensities. This observation contrasts previous reports which proposed that surface reconstructions were related to activity[7,8,10,18–20]. Here, these intermediate spatiotemporal phenomena are not related to activity, but originate from catalyst physical deformations during redox cycling.

Figure 4b shows a 3-dimensional orbit of the oscillatory dataset representing the total production rate of syngas, its first derivative of time, and the image intensities of the catalyst surface, respectively. DRM deactivation/surface oxidation cycles (instant 1 ◊ instant 2) followed a narrow trajectory of low data points dispersion during the oscillations. In contrast, activation/surface reduction (instant 2 ◊ instant 3) exhibited high dispersion and separation of data points characteristic of accelerated transits. Furthermore, the orbit is not planar, but it is bent at a given threshold of image intensities, indicating that part of the dynamics had remained hidden from OSEM imaging due to oxide intrusion into bulk regions. Extended Data Fig. 5a corroborates the extension of oxide phasess several hundred of nanometers into the bulk. Notably, Extended Data Fig. 5b and 5c reveal a layered structure and Moiré fringes at the Ni/NiO

interlayer. The HRTEM analysis of this region presented in Extended Data Fig. 5d evinces the coexistence of nanometric-sized ill-defined phases at the interlayer. In addition, multiple reflections appear around the main Fast Fourier Transform (FFT) frequencies of the cubic metallic lattice at the substrate. The partial mismatch after indexing of FFT patterns with Ni (fcc and hcp) or NiH_x points to local structural distortions. Although the average ordering of the metallic lattice was kept, regular displacements of atomic positions with respect to the ideal structure were introduced. These observations point to the presence of mechanical strain at the metallic substrate[21–24].

Altogether, our results evince that CO_2 was activated preferentially on reduced Ni sites, while CH_4 was activated on oxidized sites. The same site could not activate simultaneously both molecules, but the redox dynamics changed its selectivity. CH_4 has the strongest C-H bond among hydrocarbons (439 kJ mol^{-1})[25]. Thus, its activation requires high energy sites, such as steps or kinks, which are scarce on flat metallic surfaces (Fig. 1). Co-feed of CO_2 was needed to form high energy sites able to cleave this bond. Furthermore, water only formed during fast surface reduction (instant 2 ◊ instant 3), indicating shifts from purely DRM selectivity during the redox transition. Subsurface layers were actively involved in the ongoing cycling. These observations and the fact that C-containing species were absent during the reaction are incompatible with DRM models based on largely accepted Langmuir-Hinshelwood mechanisms[26]. Instead, they provide experimental evidence that the product selectivity was conditioned by the degree of catalyst oxidation (Eq. 1–5):

$CO_2 + nNi \rightarrow (n-1)Ni + NiO + CO$ Dissociative adsorption of CO_2 1

$CH_4 + mNiO \rightarrow (m-1)NiO + Ni + CO + 2H_2$ Partial oxidation of CH_4 2

$CH_4 + mNiO \rightarrow (m-2)NiO + 2Ni + CO + H_2 + H_2O$ Partial oxidation of CH_4 3

$CH_4 + mNiO \rightarrow (m-3)NiO + 3Ni + CO + 2H_2O$ Partial oxidation of CH_4 4

$CH_4 + mNiO \rightarrow (m-4)NiO + 4Ni + CO_2 + 2H_2O$ Total oxidation of CH_4 5

Relative rates of products formation and surface redox dynamics stemmed from the balance between CO_2 (Eq. 1) and CH_4 activations (Eq. 2–5), involving a complex reaction network governing selectivities (Extended Data Fig. 6). When the catalyst was oxidized by Eq. 1, CO formation dominated (instant 1 ◊ instant 2) leading to deactivation and decreasing H_2/CO ratios. Subsequently, the catalyst was reduced by Eq. 2–5, leading to enhanced H_2 and H_2O productivities. In this way, the catalyst sequentially created activation sites for each reactant.

Catalytic oscillations require a feedback element that flips reaction paths overtime. We propose that the trade-off between mechanical strain at the catalyst and the relative rates of the ongoing reactions (Figs. 3, 4, Extended Data Figs. 4–6, Videos 1 and 2) caused the periodic flips between the various paths. The mol volume of NiO (11.20 cm^3mol^{-1}) is 70% larger compared to metallic Ni (6.67 cm^3mol^{-1})[27].

Hence, growth of NiO pushes the underlying metallic substrate and displaces its atomic positions. This generates a restoring force in the material according to Hooke's law (Eq. 6, Supplementary Information). This effect has been demonstrated in other systems, including exsolving of Ni from archetypical $LaNiO_3$ perovskite[28]. The exsolved phase distorted the lattice parameter of the remaining La_2O_3. Recent studies have highlighted the impact of mechanical strain on the activity of metallic catalysts subjected to different loads[29–34]. "Squeezing" the catalyst is another mean of selectivity control[35].

Because long-range synchronization is needed to generate macroscopic oscillations, we rationalize these conjectures with a mean-field approach to the reaction kinetics (SI)[36,37]. Figure 4c depicts a collection of the numerical solutions calculated for a set of kinetic constants found by iteration from starting values taken from the literature[38,39]. We assumed isothermal conditions, in line with the small temperature variations detected during the oscillations. The calculated traces reproduced reasonably well the most relevant features of the experimental results (Figs. 4c, 4d).

Redox dynamics controlled catalytic performance by generation of selective activation sites and strain. This effect was only observable when the relative rates of the various phenomena were large enough for detection, which in our case occurred close to the reaction-induced transition. At different conditions, for instance at temperatures excessively high, this effect could be hidden by convolution of relatively small rate modulations superimposed by very fast turnover rates. Evaluations in such regimes could lead to the erroneous conclusion of a static catalyst operation (Table 2). The proposed "strain model" extracted from our operando approaches may explain more general observations, such as the deformation of the surface (reconstructions, faceting) and the alteration of sticking probabilities of chemical species (selectivity shifts) as the material accumulates and releases strain[31,40].

2. Conclusions

In summary, our correlative OSEM/NAP-XPS study served to elucidate the intricate influence of catalytic dynamics on reaction performance. In particular, we evinced that adsorption sites for CH_4 and CO_2 are chemically different during DRM. While CO_2 can adsorb on metallic Ni sites, CH_4 requires in situ generated oxides. This is a noticeable extension of the mechanistic model, in which adsorption centers were assumed to be common. The discussed oscillations represent the temporal separation of catalyst oxidation and reduction steps achieved by fine rate couplings, enabling a detailed picture of catalytic functioning. The generation of strain during redox cycling was proposed as a feedback element for the oscillations. We also found that surface reconstructions in particular did not account for activity. Altogether, our study highlights the importance of operando investigations to extend our knowledge on heterogeneous catalysis and fuel novel designs based on mechanistic understanding.

3. Main References

1. Ertl, G. Molecules at Surfaces: 100 Years of Physical Chemistry in Berlin-Dahlem. Angewandte Chemie International Edition 52, 52–60, doi:https://doi.org/10.1002/anie.201205401 (2013).
2. Barroo, C., de Bocarmé, T. V., De Decker, Y. & Kruse, N. in Encyclopedia of Interfacial Chemistry (ed Klaus Wandelt) 251–260 (Elsevier, 2018).
3. Beck, A. et al. The dynamics of overlayer formation on catalyst nanoparticles and strong metal-support interaction. Nature Communications 11, 3220, doi:10.1038/s41467-020-17070-2 (2020).
4. Vendelbo, S. B. et al. Visualization of oscillatory behaviour of Pt nanoparticles catalysing CO oxidation. Nature Materials 13, 884–890, doi:10.1038/nmat4033 (2014).
5. Helveg, S. et al. Observing gas-catalyst dynamics at atomic resolution and single-atom sensitivity. Micron 68, 176–185, doi:https://doi.org/10.1016/j.micron.2014.07.009 (2015).
6. Denny, N. R., Li, F., Norris, D. J. & Stein, A. In situ high temperature TEM analysis of sintering in nanostructured tungsten and tungsten–molybdenum alloy photonic crystals. Journal of Materials Chemistry 20, 1538–1545, doi:10.1039/B918423F (2010).
7. Ertl, G., Norton, P. R. & Rüstig, J. Kinetic Oscillations in the Platinum-Catalyzed Oxidation of Co. Physical Review Letters 49, 177–180, doi:10.1103/PhysRevLett.49.177 (1982).
8. Barroo, C., Wang, Z.-J., Schlögl, R. & Willinger, M.-G. Imaging the dynamics of catalysed surface reactions by in situ scanning electron microscopy. Nature Catalysis 3, 30–39, doi:10.1038/s41929-019-0395-3 (2020).
9. Wang, Z.-J. et al. Direct Observation of Graphene Growth and Associated Copper Substrate Dynamics by in Situ Scanning Electron Microscopy. ACS Nano 9, 1506–1519, doi:10.1021/nn5059826 (2015).
10. Cao, J. et al. In situ observation of oscillatory redox dynamics of copper. Nature Communications 11, 3554, doi:10.1038/s41467-020-17346-7 (2020).
11. Huang, X. et al. Phase Coexistence and Structural Dynamics of Redox Metal Catalysts Revealed by Operando TEM. Advanced Materials 33, 2101772, doi:https://doi.org/10.1002/adma.202101772 (2021).
12. Bañares, M. A., Guerrero-Pérez, M. O., Fierro, J. L. G. & Cortez, G. G. Raman spectroscopy during catalytic operations with on-line activity measurement (operando spectroscopy): a method for understanding the active centres of cations supported on porous materials. Journal of Materials Chemistry 12, 3337–3342, doi:10.1039/B204494C (2002).
13. Chenna, S. & Crozier, P. A. Operando Transmission Electron Microscopy: A Technique for Detection of Catalysis Using Electron Energy-Loss Spectroscopy in the Transmission Electron Microscope. ACS Catalysis 2, 2395–2402, doi:10.1021/cs3004853 (2012).
14. Plodinec, M., Nerl, H. C., Girgsdies, F., Schlögl, R. & Lunkenbein, T. Insights into Chemical Dynamics and Their Impact on the Reactivity of Pt Nanoparticles during CO Oxidation by Operando TEM. ACS Catalysis 10, 3183–3193, doi:10.1021/acscatal.9b03692 (2020).
15. Vendelbo, S. B. et al. Visualization of oscillatory behaviour of Pt nanoparticles catalysing CO oxidation. Nature Materials 13, 884, doi:10.1038/nmat4033

https://www.nature.com/articles/nmat4033#supplementary-information (2014).

16. Kaichev, V. V. et al. Evolution of self-sustained kinetic oscillations in the catalytic oxidation of propane over a nickel foil. Journal of Catalysis 334, 23–33, doi:https://doi.org/10.1016/j.jcat.2015.11.009 (2016).
17. Sandoval-Diaz, L. et al. Visualizing the importance of oxide-metal phase transitions in the production of synthesis gas over Ni catalysts. Journal of Energy Chemistry 50, 178–186, doi:https://doi.org/10.1016/j.jechem.2020.03.013 (2020).
18. Colaianni, M. L. & Chorkendorff, I. Scanning-tunneling-microscopy studies of the S-induced reconstruction of Cu(100). Physical Review B 50, 8798–8806, doi:10.1103/PhysRevB.50.8798 (1994).
19. Suchorski, Y. & Rupprechter, G. Local reaction kinetics by imaging. Surface Science 643, 52–58, doi:https://doi.org/10.1016/j.susc.2015.05.021 (2016).
20. Suchorski, Y. et al. Resolving multifrequential oscillations and nanoscale interfacet communication in single-particle catalysis. Science 372, 1314–1318, doi:10.1126/science.abf8107 (2021).
21. Abedi, H. R., Zarei Hanzaki, A., Nemati, N. & Kim, D.-E. Trading off between dynamic strain aging and substructure evolution in κ-carbide-free lightweight steel at room temperature. Scripta Materialia 157, 110–114, doi:https://doi.org/10.1016/j.scriptamat.2018.07.044 (2018).
22. Liang, Z. Y. & Huang, M. X. Deformation twinning in small-sized face-centred cubic single crystals: Experiments and modelling. Journal of the Mechanics and Physics of Solids 85, 128–142, doi:https://doi.org/10.1016/j.jmps.2015.09.004 (2015).
23. Kovarik, L. et al. Microtwinning and other shearing mechanisms at intermediate temperatures in Ni-based superalloys. Progress in Materials Science 54, 839–873, doi:https://doi.org/10.1016/j.pmatsci.2009.03.010 (2009).
24. Cooper, D., Denneulin, T., Bernier, N., Béché, A. & Rouvière, J.-L. Strain mapping of semiconductor specimens with nm-scale resolution in a transmission electron microscope. Micron 80, 145–165, doi:https://doi.org/10.1016/j.micron.2015.09.001 (2016).
25. Blanksby, S. J. & Ellison, G. B. Bond Dissociation Energies of Organic Molecules. Accounts of Chemical Research 36, 255–263, doi:10.1021/ar020230d (2003).
26. Sandoval-Diaz, L. E., Schlögl, R. & Lunkenbein, T. Quo Vadis Dry Reforming of Methane? A Review on Its Chemical, Environmental, and Industrial Prospects. Catalysts 12, doi:10.3390/catal12050465 (2022).
27. Haynes, W.M., Lide, D.R., Bruno, T.J., CRC Handbook of Chemistry and Physics 2016–2017: A Ready-reference Book of Chemical and Physical Data. 97th Edition. (2016).
28. Cao, P. et al. Atomic-Scale Insights into Nickel Exsolution on LaNiO3 Catalysts via In Situ Electron Microscopy. The Journal of Physical Chemistry C 126, 786–796, doi:10.1021/acs.jpcc.1c09257 (2022).
29. Du, M., Cui, L., Cao, Y. & Bard, A. J. Mechanoelectrochemical Catalysis of the Effect of Elastic Strain on a Platinum Nanofilm for the ORR Exerted by a Shape Memory Alloy Substrate. Journal of the

American Chemical Society 137, 7397–7403, doi:10.1021/jacs.5b03034 (2015).

30. He, T. et al. Mastering the surface strain of platinum catalysts for efficient electrocatalysis. Nature 598, 76–81, doi:10.1038/s41586-021-03870-z (2021).
31. Nagy, A. J. et al. The Correlation of Subsurface Oxygen Diffusion with Variations of Silver Morphology in the Silver–Oxygen System. Journal of Catalysis 182, 417–429, doi:https://doi.org/10.1006/jcat.1998.2388 (1999).
32. Nilsson Pingel, T., Jørgensen, M., Yankovich, A. B., Grönbeck, H. & Olsson, E. Influence of atomic site-specific strain on catalytic activity of supported nanoparticles. Nature Communications 9, 2722, doi:10.1038/s41467-018-05055-1 (2018).
33. Westsson, E., Picken, S. & Koper, G. The effect of lattice strain on catalytic activity. Chemical Communications 55, 1338–1341, doi:10.1039/C8CC09063G (2019).
34. Francis, M. F. & Curtin, W. A. Mechanical work makes important contributions to surface chemistry at steps. Nature Communications 6, 6261, doi:10.1038/ncomms7261 (2015).
35. Lobato, A., Salvadó, M. A., Recio, J. M., Taravillo, M. & Baonza, V. G. Highs and Lows of Bond Lengths: Is There Any Limit? Angewandte Chemie International Edition 60, 17028–17036, doi:https://doi.org/10.1002/anie.202102967 (2021).
36. Khrustova, N., Veser, G., Mikhailov, A. & Imbihl, R. Delay-Induced Chaos in Catalytic Surface Reactions: NO Reduction on Pt(100). Physical Review Letters 75, 3564–3567, doi:10.1103/PhysRevLett.75.3564 (1995).
37. Bassett, M. R. & Imbihl, R. Mathematical modeling of kinetic oscillations in the catalytic CO oxidation on Pd(110): The subsurface oxygen model. The Journal of Chemical Physics 93, 811–821, doi:10.1063/1.459451 (1990).
38. Delgado, K. H. et al. Surface Reaction Kinetics of Steam- and CO2-Reforming as Well as Oxidation of Methane over Nickel-Based Catalysts. Catalysts 5, doi:10.3390/catal5020871 (2015).
39. Maier, L., Schädel, B., Herrera Delgado, K., Tischer, S. & Deutschmann, O. Steam Reforming of Methane Over Nickel: Development of a Multi-Step Surface Reaction Mechanism. Topics in Catalysis 54, 845, doi:10.1007/s11244-011-9702-1 (2011).
40. Schlögl, R. & Abd Hamid, S. B. Nanocatalysis: Mature Science Revisited or Something Really New? Angewandte Chemie International Edition 43, 1628–1637, doi:https://doi.org/10.1002/anie.200301684 (2004).

4. Tables

Table 1
A qualitative summary of different reactions regimes for mechanistic insights

Reaction temperature	Catalytic dynamics	Reaction performance	Suitability for investigation of dynamics-performance correlation
T < phase transition	oxidized surface	little activity	none
Phase transition	oscillatory	tuned activity	very high
T > phase transition	reduced surface	very high activity	low

5. Materials And Methods

5.1 Operando SEM setup

Our setup features a quartz tube reactor inside the chamber of a commercially available environmental SEM (ESEM, FEI 200 Quanta FEG) lined to a quadrupole mass spectrometer (QMS, 200 Prisma Pfeiffer)[1]. Changes at the catalyst and in gas phase compositions are determined simultaneously, enabling the direct investigation of the influence of catalytic dynamics on performance. Our OSEM resembles a flow reactor that reproduces the flow pattern of laboratory and industrial scale systems, maximizes contact points between gas and solid phases, enables calibrations of gas compositions, and prevents contaminations stemming from the ESEM chamber environment. Temperature and gas phase compositions were controlled during surface imaging. We used a metallic Ni catalyst (foil or foam, 99.5% purity, Goodfellow) onto which a K-type thermocouple was spot-welded. Pure gases (Westfalen 5.0) were dosed into the quartz tube reactor by individual mass-flow controllers (Bronckhorst).

Images of the catalyst surface were acquired every 17.5 s with the Large Field Detector (LFD) of the ESEM at acceleration voltages of 7.5–10 kV and a chamber pressure of 16 Pa. In operando mode, catalytic rates of conversion and product selectivities were measured simultaneously to surface imaging[1].

5.2 OSEM reference tests

Samples of the Ni catalyst (metallic foam, 35 mg) were treated for 1200 minutes at 820°C in an atmosphere composed of H_2 = 0.6 $ml_N min^{-1}$ and Ar = 0.3 $ml_N min^{-1}$. The chamber pressure was 16 Pa. Afterwards, the atmosphere composition was switched to either CO_2 = 0.6 $ml_N min^{-1}$ and Ar = 0.3 $ml_N min^{-1}$, or CH_4 = 0.6 $ml_N min^{-1}$ and Ar = 0.3 $ml_N min^{-1}$. ESEM video-frames were collected during these treatments every 17.5 s.

5.3 OSEM DRM tests

After pre-treating the Ni catalyst for 1200 minutes at 820°C in an atmosphere composed of H_2 = 0.6 $ml_N min^{-1}$ and Ar = 0.3 $ml_N min^{-1}$, the H_2 flow was switched off and the reactor was cooled down to room temperature. Flows of CH_4 = 0.4 $ml_N min^{-1}$ and CO_2 = 0.3 $ml_N min^{-1}$were introduced in the reactor until gas phase compositions in the QMS traces had stabilized (time on stream = 0 min). The catalyst was heated to 700°C within 10 s, and after 30 minutes of stabilization, ESEM imaging was initiated. The reaction temperature was stepwise increased (17°C or 16°C each) from 700°C to 900°C. After 1000 minutes of treatment at 900°C, the reaction temperature was decreased to 818°C. Oscillations initiated spontaneously (time on stream = 1880 minutes), and ESEM video-frames were continually collected until the end of the experiment (time on stream = 2800 min).

During oscillations, the signal of O_2 was found to be steady and close to zero, indicating its exclusion from the dynamics. O_2 often contaminates the microscope chamber due to external leaks. Consequently, obscuring dynamics initiated by oxygen-induced hydrocarbon oxidation can cause oscillating dynamics and disrupt the chemical network (Extended data Table 1)[2].

5.4 Image treatment

Collected OSEM video-frames were treated with Fiji®[3]. The stack of video-frames was aligned with translation registration, and image intensities were normalized (10x10 $pixel^2$, 1 standard deviation) to eliminate fluctuations originating from temperature or gas compositions changes. Afterwards, average pixel intensities were plotted as a time series. Videos and selected ROIs cropped and digitally scaled from the video-frames were produced with the same software.

5.5 NAP-XPS experiments

Near-ambient-pressure X-ray photoelectron spectroscopy (NAP-XPS) measurements were performed at the UE56/2-PGM1 (Elliptical Undulator) beamline of the synchrotron radiation facility of BESSY II of Helmholtz-Zentrum Berlin (HZB), Germany. The details of the beamline layout and performance can be found elsewhere[4]. The home-built near-ambient pressure electron spectrometer is described in detail in the literature [5,6].

The nickel foam sample and a K-type thermocouple were fixed into a sapphire sample holder. The sample was mounted inside the XPS/XANES reaction cell, near to the aperture of the first differential pumping stage. The exit slit of the beamline was 180um and a pass energy of 10 eV and 0.1 eV step were used during spectra acquisition with an experimental resolution of about 0.55 eV.

The heating treatment was carried out with a near infrared laser (808 nm, max. 60W) shining at the rear of the mounting plate. Gas compositions during the measurements were monitored by a quadrupole mass spectrometer.

The catalyst was pretreated by annealing in 0.16 mbar (16 Pa) of H_2:Ar mixture at 810°C using a heating rate of 5°C min^{-1} to achieve the reduced state. The partial pressure of the gas feeds was controlled by

mass-flow controllers (Bronkhorst) and set to the values of OSEM experiments.

XP spectra of core level regions were recorded with kinetic energies of emitted photoelectrons at 130 eV and 300 eV for Ni2p, and 130 eV, 300 eV and 600 eV for O1s, C1s and Si2p.

Afterwards, spectra were acquired on the pre-reduced sample at the same pressure and temperature with gas feeds of CO_2:Ar, CH_4:Ar, and CO_2:CH_4:Ar. Each set of spectra was recorded with 60 minutes of separation between the first acquisitions to evaluate the changes over time.

XP spectra were analyzed with CasaXPS. The binding energies were calibrated to the Fermi edge of a Au reference sample. The O1s spectra were deconvoluted with combined gaussian and lorentzian functions after a Shirley + linear background subtraction.

Note that besides employing two independent operando characterization techniques (NAP XPS and OSEM) that reveal the same chemistry, operando experiments are advantageous over in situ experiments as they help precluding imaging and spectral artifacts via product-structure correlation.

5.6 Numerical fits of catalytic observables

We used a mean field approach based on a set of ordinary differential equations representing the individual rates of a redox cycle of multiple paths. The numerical solutions were achieved with motion rate law and initial conditions of gas flows representing the experimental values. The values of gaseous, surface and subsurface species over the arbitrary time (simulation ticks) series were calculated in Wolfram Mathematica[7] by a black-box reactor model with internally adjusted time constant, a contact time of 3 ticks, and a total catalyst area of 1. Values were evaluated from 0 to 500 000 simulation ticks, and then the period of the oscillating traces was rescaled to fit our experimental traces (93 mins).

5.7 Focus Ion Beam (FIB) lamella preparation and HRTEM imaging

A TEM lamella of the spent catalyst was prepared with an FEI Helios NanoLab G3 FIB/SEM system using Ga ions with energies up to 30 keV. A Pt-C protective layer of 600 nm thickness was added to the catalyst surface by electron beam induced deposition. Additional 600 nm of carbon were deposited by focus ion beam, and the lamella was thinned from both sides to < 100 nm by a 30 kV Ga ion beam. Afterwards, low energy ion beams of 5 kV and 2 kV were applied to the sidewalls of the lamella. The lamella was mounted in the FIB onto a TEM Cu grid and examined at RT with a double aberration-corrected JEOL JEM-ARM 200CF TEM at 200 kV and an emission current of 10.0 µA. The identification of the dominant crystalline phases was performed with the CrysTBox package[8]. Reflections obtained during the Fast Fourier transform (FFT) analysis of the HRTEM images were fitted to known references.

6. Methods References

1. Sandoval-Diaz, L. et al. Visualizing the importance of oxide-metal phase transitions in the production of synthesis gas over Ni catalysts. Journal of Energy Chemistry 50, 178–186, doi:https://doi.org/10.1016/j.jechem.2020.03.013 (2020).
2. Kaichev, V. V. et al. Evolution of self-sustained kinetic oscillations in the catalytic oxidation of propane over a nickel foil. Journal of Catalysis 334, 23–33, doi:https://doi.org/10.1016/j.jcat.2015.11.009 (2016).
3. Schindelin, J. et al. Fiji: an open-source platform for biological-image analysis. Nature Methods 9, 676–682, doi:10.1038/nmeth.2019 (2012).
4. Sawhney, K. J. S. et al. A novel undulator-based PGM beamline for circularly polarised synchrotron radiation at BESSY II. Nuclear Instruments and Methods in Physics Research Section A: Accelerators, Spectrometers, Detectors and Associated Equipment 390, 395–402, doi:https://doi.org/10.1016/S0168-9002(97)00402-6 (1997).
5. Knop-Gericke, A. et al. in Advances in Catalysis Vol. 52 213–272 (Academic Press, 2009).
6. Salmeron, M. & Schlögl, R. Ambient pressure photoelectron spectroscopy: A new tool for surface science and nanotechnology. Surface Science Reports 63, 169–199, doi:https://doi.org/10.1016/j.surfrep.2008.01.001 (2008).
7. Mathematica (Wolfram Research, Inc., Champaign, Illinois, 2018).
8. Klinger, M. & Jäger, A., Crystallographic Tool Box (CrysTBox): automated tools for transmission electron microscopists and crystallographers, Journal of Applied Crystallography 48, 2012–2018, https://doi.org/10.1107/S1600576715017252 (2015).

7. End Notes

Data availability

The data that support the findings of this study are available from the Data Archive of the Fritz Haber Institute of the Max Planck Society, https://ac.archive.fhi.mpg.de/D55435. Further data presented in the Extended Data are available from the corresponding authors upon reasonable request.

Code availability

The Wolfram Mathematica code for the microkinetic fit is available from the Data Archive of the Fritz Haber Institute of the Max Planck Society, https://ac.archive.fhi.mpg.de/D55435.

Acknowledgement

We are grateful to the Federal Ministry of Education and Research in the framework of the project Catlab (03EW0015A). Helmholtz-Zentrum Berlin is also acknowledged for providing beamtime in the frame of proposal ID 191-08444 and for the continuous support of the (near) ambient pressure XPS activities of the MPG at the synchrotron light source BESSY II, Germany.

Author contributions

T.L., R.S., and A.K-G. conceived the project. L.S.D. and D.I. constructed the OSEM setup and carried out the OSEM experiments. L.S.D., D.C., T.G. and M.H. carried out the NAP-XPS experiments. A.H. prepared the catalyst cross-section by FIB. M.P. analyzed the cross-section sample by HRTEM imaging. L.S.D., D.C. and T.L. analyzed the operando spectromicroscopy and post-reaction data. L.S.D. calculated the numerical fittings. L.S.D. and T.L. wrote the manuscript. T.L., R.S., and A.K-G. guided the research. All authors discussed the results and commented the manuscript.

Competing interest declaration

The authors declare no competing interests.

Figures

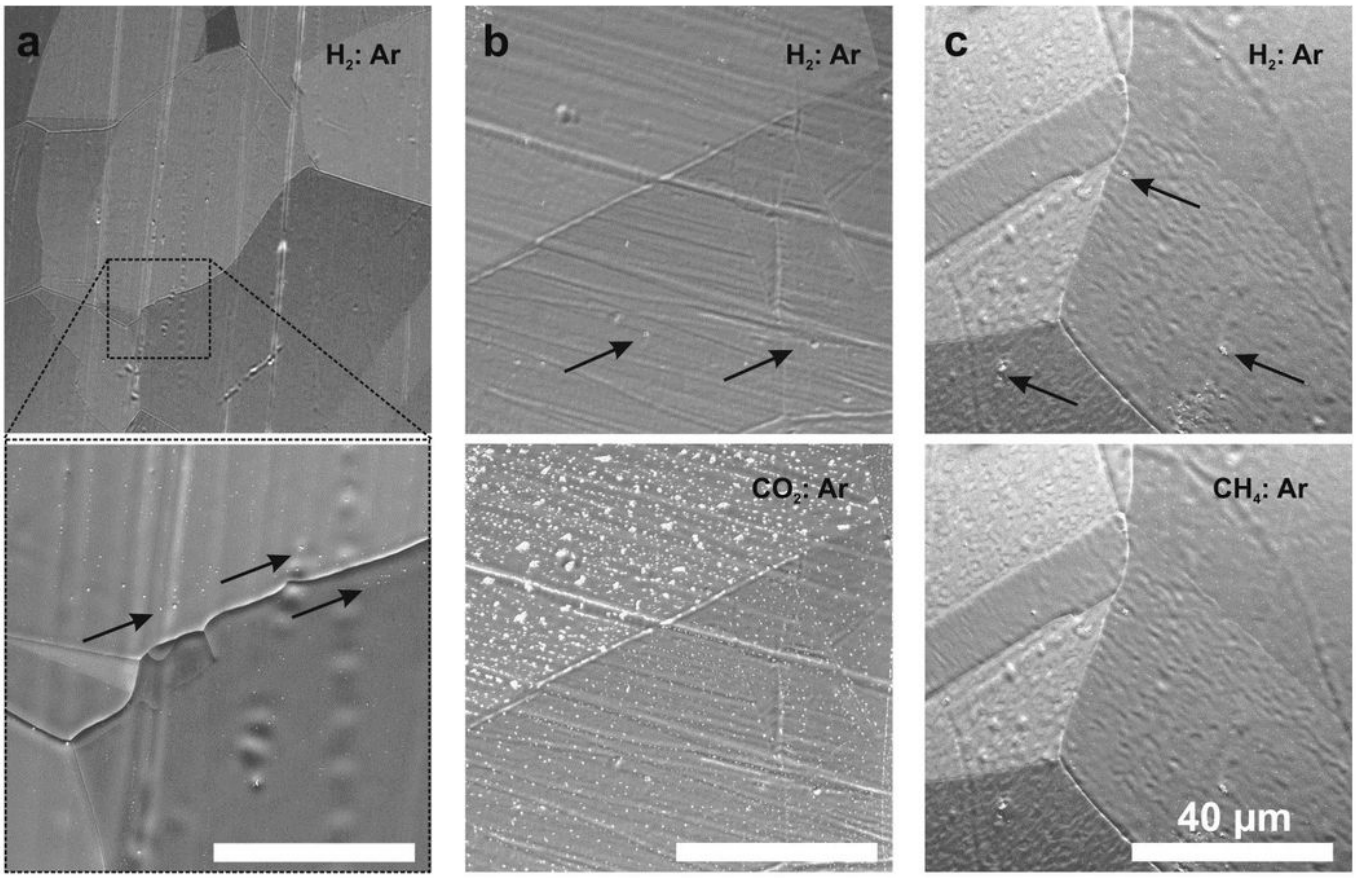

d

Figure	Top panel gas flow values in $ml_N min^{-1}$. Reaction temperature: 820 °C. Reaction pressure: 16 Pa				Bottom panel gas flow values in $ml_N min^{-1}$. Reaction temperature: 820 °C. Reaction pressure: 16 Pa			
	H_2	CO_2	CH_4	Ar	H_2	CO_2	CH_4	Ar
1a	0.60	--	--	0.30	0.60	--	--	0.30
1b	0.60	--	--	0.30	--	0.60	--	0.30
1c	0.60	--	--	0.30	--	--	0.60	0.30

Figure 1

Catalyst sate dependency on gas environment. a, **top:** In situ SEM image of the H_2 reduced Ni catalyst. **a, bottom:** A magnified region of interest (ROI) of **a, top**. Conditions of acquisition for **a**: Gas mixture composed of 0.3 $ml_N min^{-1}$ Ar, 0.6 $ml_N min^{-1}$ H_2, 1200 minutes of exposure to the feed. **b**, **top:** In situ SEM image of the H_2 reduced Ni catalyst. Conditions of acquisition for **b, top**: Gas mixture composed of 0.3

$ml_N min^{-1}$ Ar, 0.6 $ml_N min^{-1}$ H_2 , 1200 minutes of exposure to the feed. **b, bottom:** Effect of switching the H_2 flow into CO_2. Bright features appeared at the catalyst. Conditions of acquisition of **b, bottom**: Gas mixture composed of 0.3 $ml_N min^{-1}$ Ar, 0.6 $ml_N min^{-1}$ CO_2, 30 minutes of exposure to the feed. **c, top:** In situ SEM image of the H_2 reduced Ni catalyst. Conditions of acquisition for **c, top**: Gas mixture composed of 0.3 $ml_N min^{-1}$ Ar, 0.6 $ml_N min^{-1}$ H_2 , 1200 minutes of exposure to the feed. **c, bottom:** Effect of switching the H_2 flow into CH_4. No changes are evident at the catalyst. Conditions of acquisition of **c, bottom**: Gas mixture composed of 0.3 $ml_N min^{-1}$ Ar, 0.6 $ml_N min^{-1}$ CH_4, 30 minutes of exposure to the feed. Reaction temperature: 820 °C. Reaction pressure: 16 Pa. Scale bar= 40μm. Arrows show features which remained during the treatments. **d**. Illustration of acquisition conditions for Figures 1a-1c in OSEM and Extended Data Figure 1.

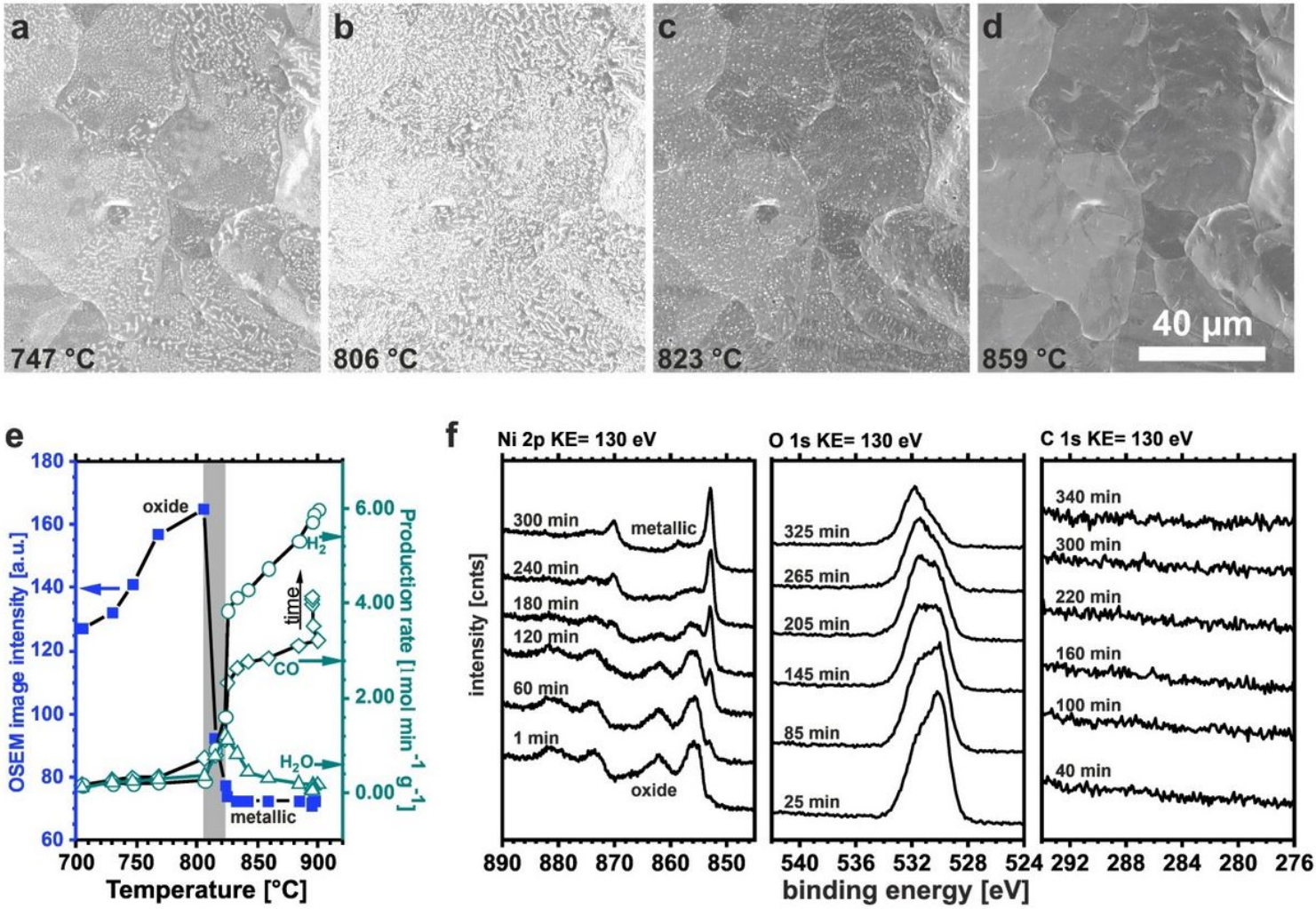

Figure 2

The importance of the redox transition for catalytic activation. a-d, Consecutive OSEM images of the Ni surface collected in the DRM mixture as a function of reaction temperature. Conditions of acquisition for **a-d**: Gas mixture composed of 0.3 $ml_N min^{-1}$ Ar, 0.3 $ml_N min^{-1}$ CO_2, 0.4 $ml_N min^{-1}$ CH_4. Scale bar= 40μm. **e,** Collection of observables of OSEM during DRM as a function of reaction temperature. The gray area

represents the interval of reaction-induced phase transition and catalytic activations. Reevaluated from reference [17]. **f,** NAP XP spectra of Ni 2p, O 1s and C 1s core levels at kinetic energies (KE) of 130 eV in the DRM feed at 810 °C. Spectra from bottom to top are equally separated by 60 minutes. Conditions of acquisition: Gas mixture composed of 0.3 $ml_N min^{-1}$ Ar, 0.3 $ml_N min^{-1}$ CO_2, 0.4 $ml_N min^{-1}$ CH_4. Reaction pressure: 16 Pa.

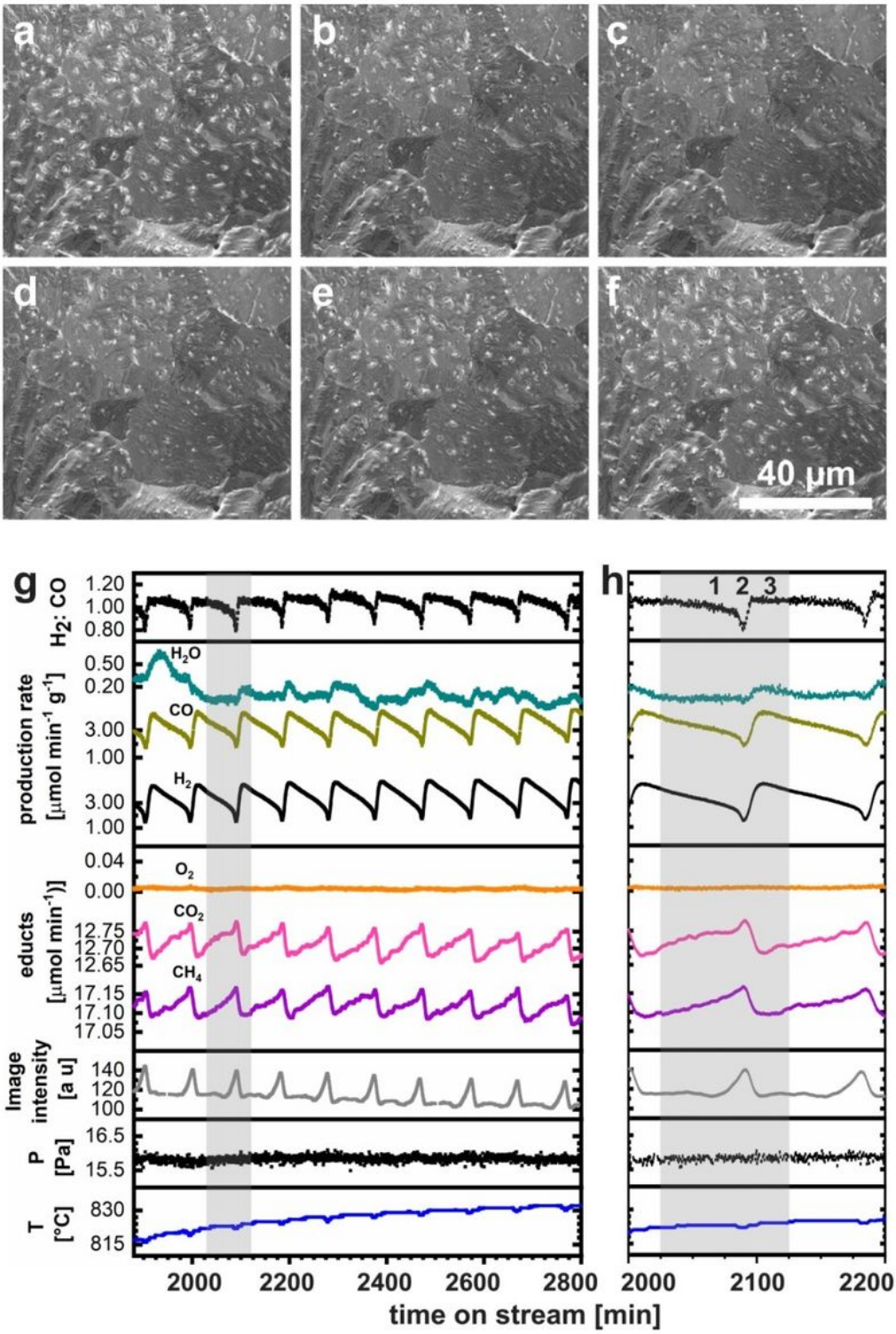

Figure 3

Self-sustained oscillations featuring reversible redox transitions. a-c, Consecutive OSEM images of the catalyst surface during oxides shrinkage of an oscillation. **d-f**, Consecutive OSEM images of the catalyst surface during oxide growth of an oscillation. Scale bar= 40µm. **g**, Time series of simultaneously recorded sample temperature, chamber pressure, OSEM image intensities, and traces of reactants and products detected by online mass spectrometry during the oscillations. **h**, A magnified portion of the dataset presented in **g**. Conditions of acquisition: Gas mixture composed of 0.3 $ml_N min^{-1}$ Ar, 0.3 $ml_N min^{-1}$ CO_2, 0.4 $ml_N min^{-1}$ CH_4.

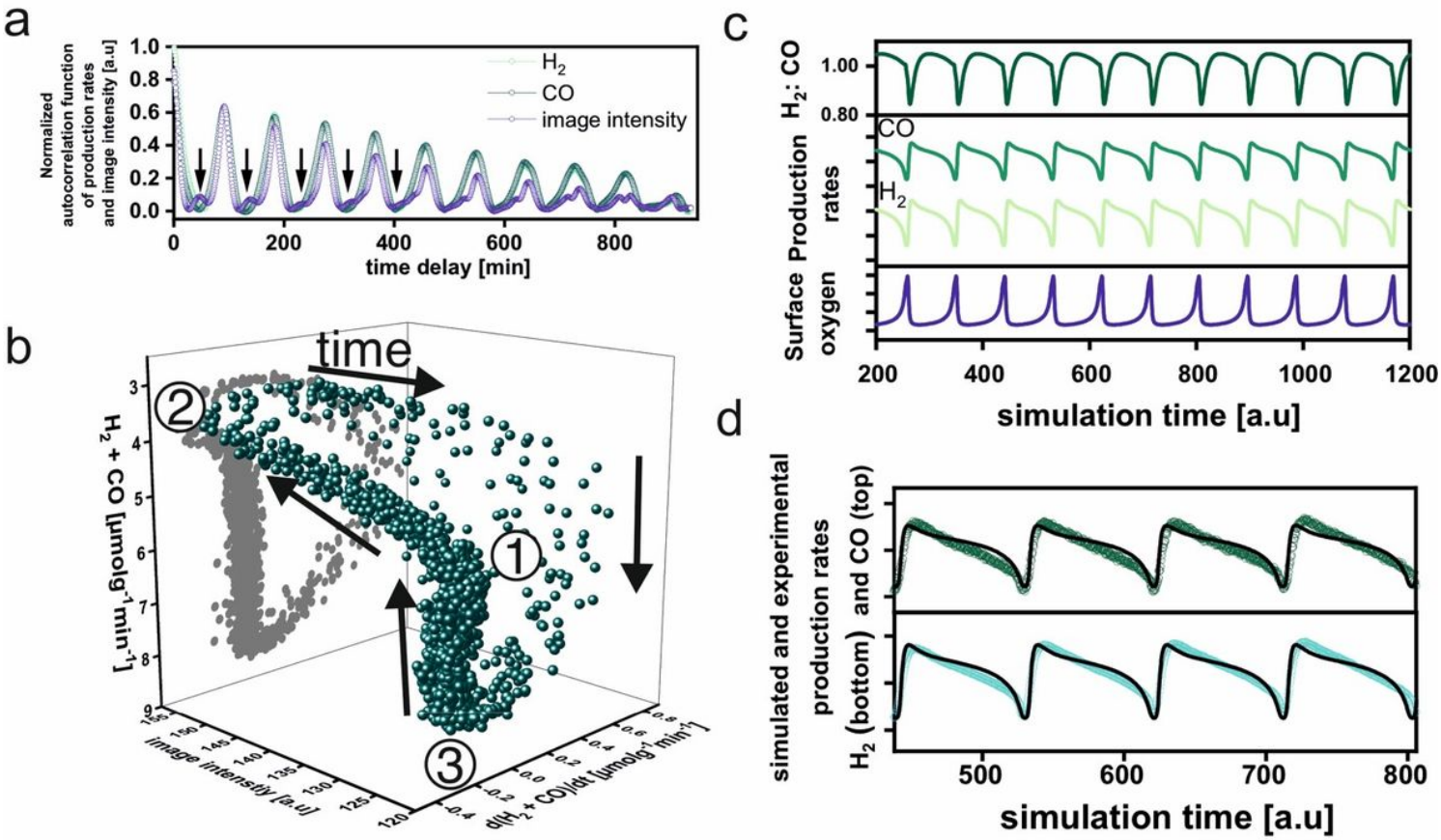

Figure 4

Dynamics-activity correlations during the oscillations of DRM. a, Normalized autocorrelation functions of H_2, CO and OSEM image intensity traces during the oscillations. Arrows show intermediate signals in image intensity trace. **b**, Orbit of the oscillating reaction in a space formed by image intensities, production rates of H_2 and CO, and the time derivatives of production rates. **c**, Numerical solutions of the proposed model for the oscillations of DRM. **d,** A comparison of calculated and experimental traces during the oscillations.

Supplementary Files

This is a list of supplementary files associated with this preprint. Click to download.

- ExtendedDataVideo2.MagnifiedROIsoftheoscillatingcatalystsurface..mp4
- ExtendedDataVideo1.OscillationsoftheNicatalystduringDRMasdetectedbyOSEM.mp4
- ExtendedDataandSupplementaryInformation.docx